Science Advances

AAAS

advances.sciencemag.org/cgi/content/full/4/3/eaap9861/DC1

Supplementary Materials for

Asymmetric photon transport in organic semiconductor nanowires through electrically controlled exciton diffusion

Qiu Hong Cui, Qian Peng, Yi Luo, Yuqian Jiang, Yongli Yan, Cong Wei, Zhigang Shuai, Cheng Sun, Jiannian Yao, Yong Sheng Zhao

Published 16 March 2018, *Sci. Adv.* **4**, eaap9861 (2018)
DOI: 10.1126/sciadv.aap9861

This PDF file includes:

section S1. Calculation of BPEA excitons

Frenkel excitons in organic materials normally possess high binding energy (*37*) and large oscillator strength. These excitons are highly stable even at room temperature. We calculated the exciton binding energy by using an accurate approach (E_b=IP-EA-E_{ex}) with considering polarizable effect (*38*). Here, we optimized the geometrical structures of neutral molecule in the ground and first excited states, as well as those of the cation and anion molecules, and obtained their total electronic energies at b3lyp/6-31+g(d) level in the framework of the polarizable continuum model. The ionization potential (IP, IP= E(cation) - E(neutral)), electron affinity (EA, EA=E(anion)-E(neutral)), and the lowest adiabatic excitation energy of BPEA crystal were achieved as 5402 meV, 2630 meV, and 2120 meV, respectively, resulting in an exciton binding energy in solid state of 652 meV. Because this binding energy is much larger than kT (30 meV) at room temperature, the excitons in BPEA nanowire should be stable with large diffusion length.

section S2. Preparation and structural characterization of BPEA nanowires

The molecular structure of BPEA is shown in fig. S1. The planar molecules can be arranged tightly in a packed crystal structure with an intermolecular distance of as short as 3.37 Å (Fig. 1A), resulting in the strong exciton-photon coupling and large coherent exciton diffusion length (*39*, *40*). Therefore, the choice of BPEA for constructing the nanostructures will ensure the efficient electrically controlled exciton diffusion to realize asymmetric optical out-coupling.

The BPEA nanowires were fabricated by a physical vapor transport technique. Pure BPEA powder (Sigma Aldrich) was heated to its sublimation temperature in an argon flow (99.999% purity, 100 s.c.c.m.) in a quartz tube oven. The Si/SiO_2 substrates were placed at the downstream side of the flowing argon for product collection. The diameter ratio and the length of the BPEA wires can be tuned by altering the preparation conditions. Longer wires can be obtained by slowing down the cooling rate, and the diameter increases at increasing evaporation temperatures.

SEM image in fig. S2 reveals that the as-prepared nanostructures have uniform 1D wire-like morphology with very smooth surfaces. The BPEA nanowires show very similar absorption and photoluminescence spectra with those of the BPEA powder (fig. S3), which indicates that the BPEA does not undergo chemical reaction during the vapor transportation. The atomic force microscopy (AFM) image (fig. S4) indicates that the wires have very smooth surfaces and rectangular cross section. The contrast between the XRD pattern of BPEA nanowires and that of the powder sample are displayed in fig. S5, which indicates the high crystallinity of the wires. The identical selected area electron diffraction (SAED) patterns from different areas of the wire in fig. S6 show that the prepared nanowires have a close packed crystalline structure with smooth surfaces growing along the [010] direction. Figure S7 illustrates the crystal packing of BPEA molecules, showing the closely packed herringbone structure. The excellent crystallinity and π-stacking of the conjugated molecules would improve the exciton-photon coupling and the migration of excitons during the light guiding process.

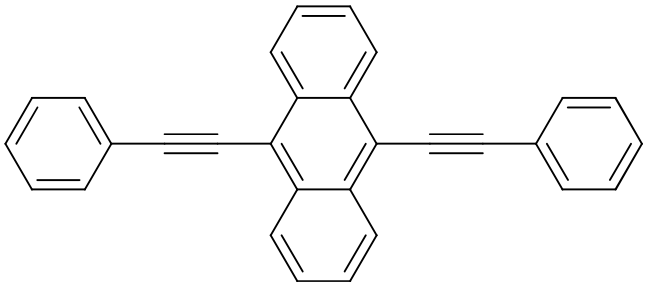

fig. S1. Molecular structure of BPEA.

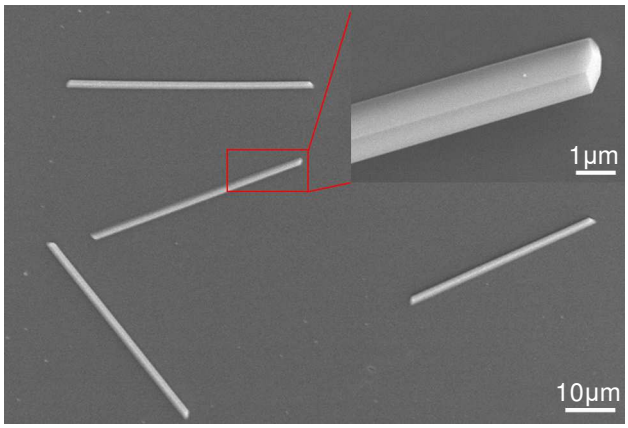

fig. S2. Scanning electron microscopy (SEM) image of the BPEA nanowires. Inset shows the magnified view of the nanowire end with a smooth and flat surface. The smooth surfaces and defect-free structures are beneficial to the photoluminescence (PL) energy propagation along the wires. For most typical samples, the error range of the length is ± 500 nm, while that of the width is ± 100 nm.

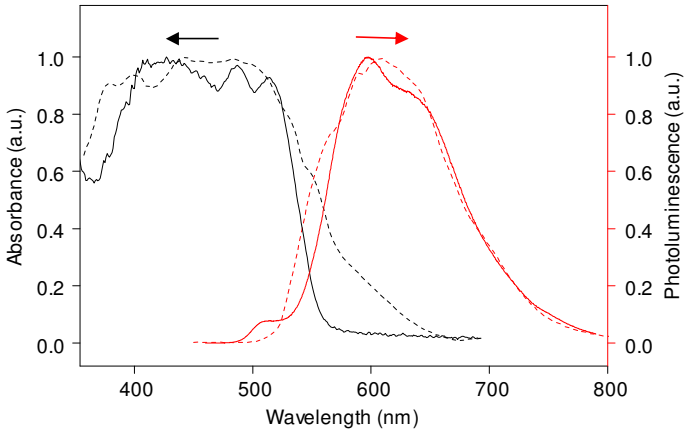

fig. S3. Absorption and fluorescence (solid) spectra of BPEA powder (black) and BPEA nanowires (red). The BPEA nanowires show very similar absorption and photoluminescence spectra with those of the BPEA powder, which indicates that the BPEA does not undergo chemical reaction during the vapor transportation.

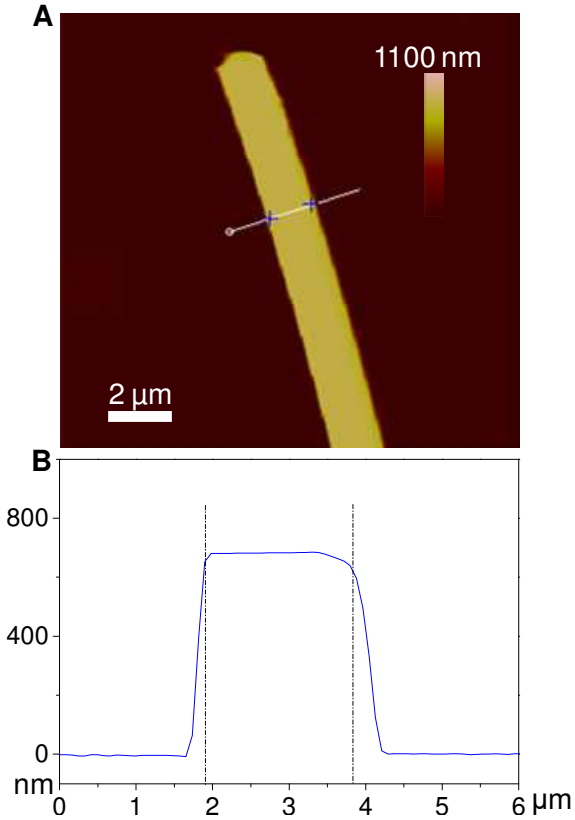

fig. S4. Atomic force microscope (AFM) characterization for a single BPEA nanowire. AFM image (**A**) and (**B**) the corresponding cross section profile of a single BPEA nanowire. The results demonstrate the flatness of the surface and the rectangular shape of the cross section.

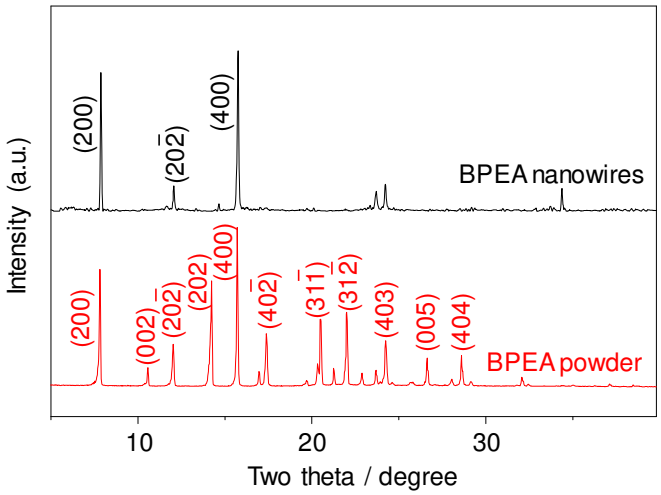

fig. S5. XRD patterns of the BPEA nanowires (black) and a monoclinic powder sample (red). The peaks in the pattern of the nanowires can be indexed to a monoclinic single crystal (space group: *C* 2/c, *a* = 22.866(5), *b* = 5.3567(11), *c* = 16.930(3), $\alpha = 90°$, $\beta = 99.72(3)°$, $\gamma = 90°$. CCDC No.: LEPPIF01).

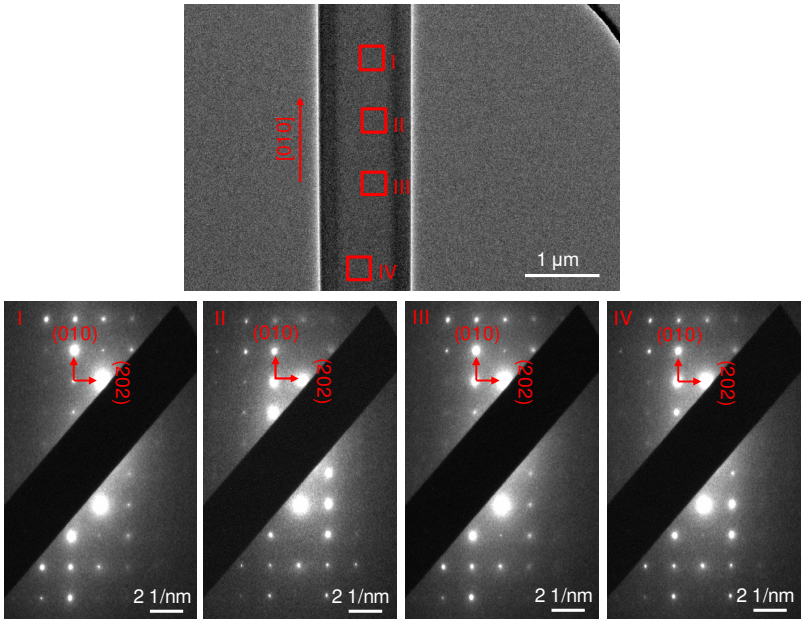

fig. S6. TEM image of BPEA nanowire and SAED patterns collected from different areas of a single wire. The identical SAED patterns from different areas of the wire indicate the perfect single crystal along the BPEA nanowire.

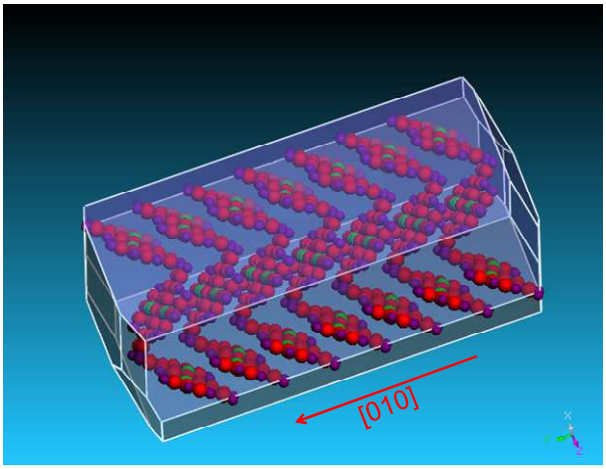

fig. S7. Thermodynamically stable molecular packing in the BPEA nanowire. It can be seen that the BPEA nanowire has a close packed herringbone 1D π-stacking of the conjugated molecules along the [010] direction (i.e. the *b* axis), which results in a large overlap between adjacent π orbitals and further improves the migration of excitons and the exciton-photon coupling.

section S3. Formation of EPs in the BPEA nanowires

The defect-free structure of the crystal nanowires ensures high photon confinement, leading to an excellent waveguide properties (*28*). PL images in Fig. 1C and fig. S8A indicate that the wires absorbed the excitation light and propagate the PL emission toward the wire tips (*41, 42)*. Optical signals were measured from the tip of a wire by accurately shifting the excitation laser spots (fig. S8B). As shown in fig. S8C, the PL intensity decays exponentially at shorter wavelengths but much slower at longer wavelengths with respect to the propagation distance. In addition, the imaginary part of the complex refractive index (*Im* (n)) reveals strong dispersion, and the energy-wavevector dispersion is distinct from the purely photonic modes, which clearly indicate the formation of EPs upon the excitation.

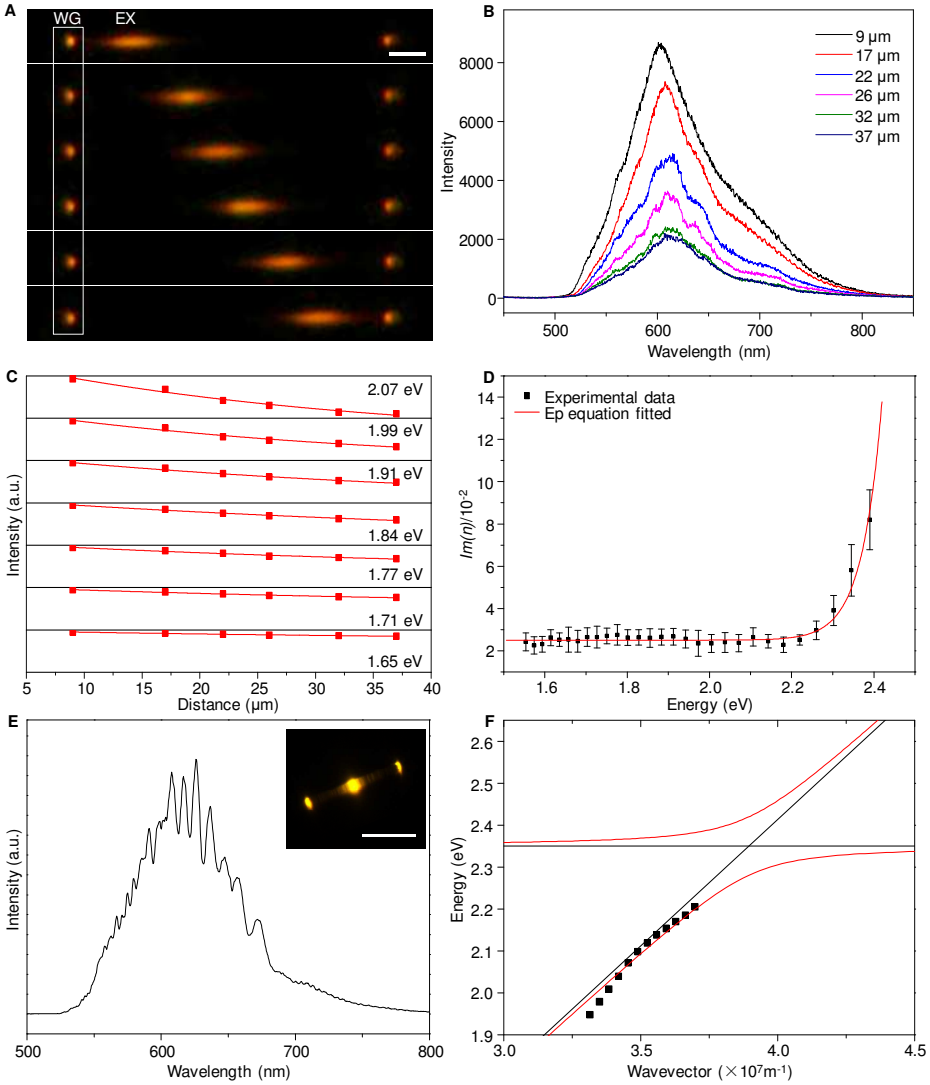

fig. S8. Formation of EPs in the BPEA nanowires. (**A**) PL images obtained from a single BPEA nanowire by exciting the wire at different positions. Scale bar is 5 μm. EX: excited spot; WG: waveguided emission. (**B**) Spatially resolved PL spectra collected from the tip (marked with white box in a) of the wire. (**C**) Decay profile of the guided PL intensity at different wavelengths. (**D**) Plot of the imaginary part of the complex refractive index (*Im* (n)) versus photon energy. Error bars represent the standard deviation of three representative measurements. (**E**) PL spectrum from the end of a wire of ~7 μm long. Inset: the PL microscopy image of the wire. Scale bar is 5 μm. The modulation in the higher energy region is less pronounced due to the photon reabsorption. (**F**) Energy-wavevector dispersion along the direction of wire axis. The square data points indicate the Fabry-Pérot peaks, which have been placed in wavevector space at integer values of π/L with L being the nanowire length.

The solid lines show the results of numerical calculations for the strong coupling between excitons and photons, resulting in avoided crossing at the exciton resonance.

To verify the EP propagation, we studied the dispersion relation of the complex refractive index (*43, 44*). First, the imaginary part of the refractive index (*Im* (n)) was determined from the decay of guided PL intensity shown in fig. S8C. It was calculated with the equation $I=I_0\exp[-2\omega Im\,(n)X/c]$ (*27*), where I_0 is the PL intensity at the excited spot, ω is the frequency of the light, X is the propagation distance, and c is the speed of light. The relationship between *Im* (n) and photon energy is plotted in fig. S8D from the optical loss versus propagation distance in fig. S8C.

Secondly, the energy-wavevector dispersion along the direction of wire axis was determined from the resonant modes in the BPEA Fabry-Pérot (FP) type resonator cavity. Here we selected a wire of ~7 μm in length (shorter than that for the asymmetric transport measurements) because the shorter wire favors the back and forth travel of photons to form the cavity modes. Figure S8E shows the emission spectrum collected from the tip of the wire under the excitation of a 351 nm laser beam. A series of PL peaks from the FP modulation in the outcoupled spectrum can be used to construct the energy-wavevector dispersion of the propagating mode by placing these peaks at integer multiples of π/L in the wavevector space (in fig. S8F). The experimental data points were analyzed with a coupled oscillator model taking into account the coupling between the exciton and the photon. The polariton states resulting from the exciton-photon interaction can be expressed as

$$E_{U,L}(k)=\left\{\left[E_{ph}(k)+E_{ex}\right]/2\right\}\pm\sqrt{\Delta^2+\left\{\left[E_{ph}(k)-E_{ex}\right]^2/4\right\}} \qquad (1)$$

where k is the in-plane wave vector, $E_U(k)$ is the energy of the upper polariton state, and $E_L(k)$ is the one of the low polariton state, E_{ex} is the energy of the exciton, E_{ph} is the energy of the photon, and Δ is an energy related to the interaction between the photon and the exciton.

It can be seen from fig. S8D and fig. S8F that the imaginary part of the complex refractive index (*Im* (n)) reveals strong dispersion, and the energy-wavevector dispersion is distinct from the purely photonic modes, indicating the formation of EPs from the strong coupling between photons and excitons.

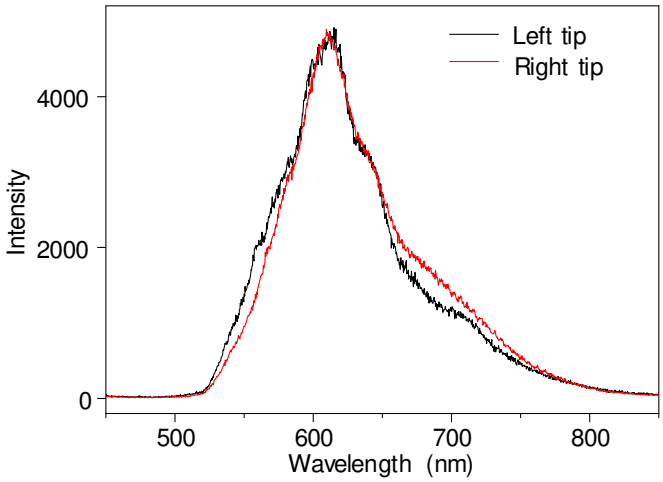

fig. S9. Output spectra from the two ends of the nanowire in Fig. 1C when the excitation is located in the middle of the wire. The results indicate that the intensities of the outcoupled emissions are almost identical, with the same propagation length to the opposite directions without electric field.

section S4. Structure of the device

The SEM image illustrates that the nanowires and electrodes form a non-intimate contact with each other, and the Cu electrodes are thick enough to ensure the application of a uniform electric field in the plane of the wires.

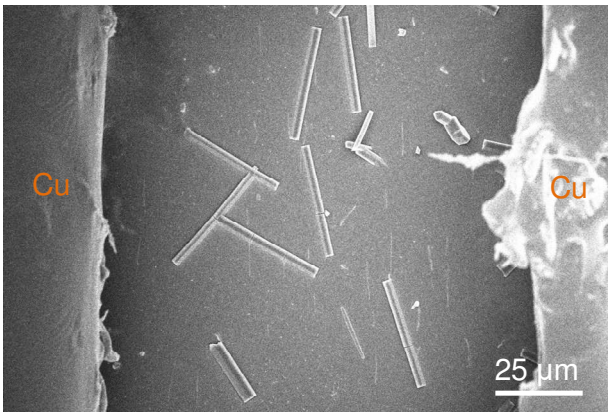

fig. S10. SEM image of a typical device.

section S5. Diffusion of the excitons under the applied electric field

The directional light propagation under the external electric field can be well illustrated by the asymmetric distribution of the exciton density and the density gradient, which can be obtained by solving the diffusion equation.

In a uniform electric field, the one-dimensional steady state exciton diffusion equation can be written as

$$\frac{d^2n(z)}{dz^2}-\frac{v}{D}\frac{dn(z)}{dz}-\frac{1}{D\tau}n(z)+\frac{1}{D}\frac{\lambda\eta}{hc}I_0\alpha e^{-\alpha|z|}=0 \qquad (2)$$

where D is the diffusion constant, v is the drift velocity that is determined by the force generated by the interaction potential, τ is the exciton lifetime, η is the quantum efficiency of the exciton generation, h is Planck constant, c is the speed of light, λ is the wave length of the incident light, I_0 is the intensity of the incident light, and α is the absorption coefficient. The general solution to eq.2 is

$$n_+(z)=\frac{\tau\theta_1 I_0\alpha}{h\upsilon-h\upsilon\alpha v\tau-Dh\alpha^2\upsilon\tau}e^{-z\alpha}+C_1e^{\frac{1}{2}z\left(\frac{v}{D}-\sqrt{\frac{4D+v^2\tau}{D^2\tau}}\right)}+C_2e^{\frac{1}{2}z\left(\frac{v}{D}+\sqrt{\frac{4D+v^2\tau}{D^2\tau}}\right)},\quad z>0 \qquad (3a)$$

$$n_-(z)=\frac{\tau\theta_1 I_0\alpha}{h\upsilon+h\upsilon\alpha v\tau-Dh\alpha^2\upsilon\tau}e^{z\alpha}+C_1e^{\frac{1}{2}z\left(\frac{v}{D}-\sqrt{\frac{4D+v^2\tau}{D^2\tau}}\right)}+C_2e^{\frac{1}{2}z\left(\frac{v}{D}+\sqrt{\frac{4D+v^2\tau}{D^2\tau}}\right)},\quad z<0 \qquad (3b)$$

Using the boundary conditions $n(z)=0$ at infinity (|z| > diffusion length), as well as $n_+(z)=n_-(z)$ and $\frac{dn_+(z)}{dz}=\frac{dn_-(z)}{dz}$ at z=0, the two constant C_1 and C_2 can be solved and the results are

$$C_1=\frac{\left(v^2\tau-2D^2\alpha^2\tau+2D+v\sqrt{4D\tau+v^2\tau^2}\right)\tau^2\lambda\alpha^2I_0\theta_1}{hc\sqrt{4D\tau+v^2\tau^2}\left(v\alpha\tau-D\alpha^2\tau+1\right)\left(v\alpha\tau+D\alpha^2\tau-1\right)} \qquad (4a)$$

$$C_2 = \frac{\left(v^2\tau - 2D^2\alpha^2\tau + 2D - v\sqrt{4D\tau + v^2\tau^2}\right)\tau^2\lambda\alpha^2 I_0\theta_1}{hc\sqrt{4D\tau + v^2\tau^2}\left(v\alpha\tau - D\alpha^2\tau + 1\right)\left(v\alpha\tau + D\alpha^2\tau - 1\right)} \qquad (4b)$$

To quantitatively estimate the asymmetric distribution of the exciton density and the gradient of density, we first determine the required physical parameters from quantum calculations and experiments. The radiative (k_r), non-radiative (k_{nr}) and energy transfer (k_{et}) rates of BPEA can be calculated by using the thermal vibration correlation function methods in MOMAP program (*45-47*) and the values are 1.49×10^8 s^{-1}, 8.27×10^4 s^{-1} and 3.27×10^{13} s^{-1}, respectively. The corresponding exciton lifetime is 6.72×10^{-9} s. The one-dimensional diffusion constant can be obtained to be 0.1878 cm^2/s from the relation $D=2d^2k_{et}$, (d is the intermolecular distance). The drift velocity v can be written as the product of the mobility of exciton and the electric field, $v = m_bE$. The exciton mobility can be obtained from the Einstein's relation $m_b = De/k_bT$. The other parameters η, α, I_0, λ are set as 100%, 5×10^3 cm^{-1}, 5.0×10^7 J/m^2s, and 351 nm, respectively according to the experimental conditions. Finally, the obtained exciton density and the gradient of exciton density are given in fig. S11.

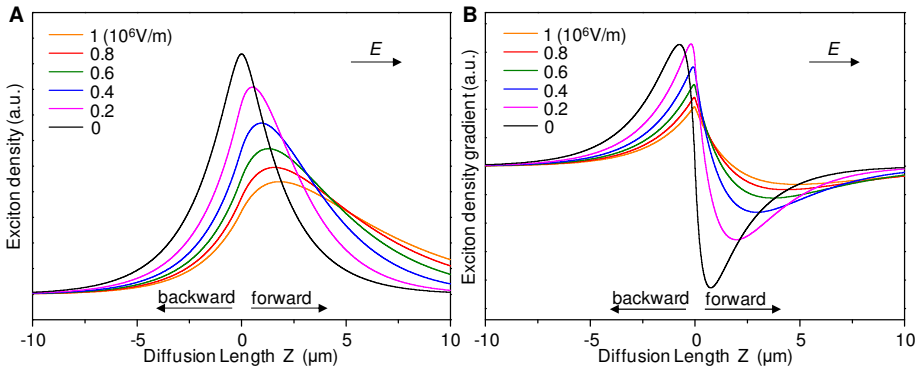

fig. S11. Calculated results of the asymmetric distribution of exciton density. Calculated exciton density profile (**A**) and exciton density gradient profile (**B**) as a function of diffusion length.

The uneven distribution of the exciton density and directional propagation are clearly demonstrated by the simulations. Our calculated results show that the directional light propagation is much extended along the direction of the electric field.

section S6. Electric effect on the passively waveguided light

The electric effect on the passively guided light is illustrated in fig. S12, which indicates that the propagated photons have no response to the electric field, and confirms that the photon transport asymmetry is based on the response of the excitonic portion of the EPs.

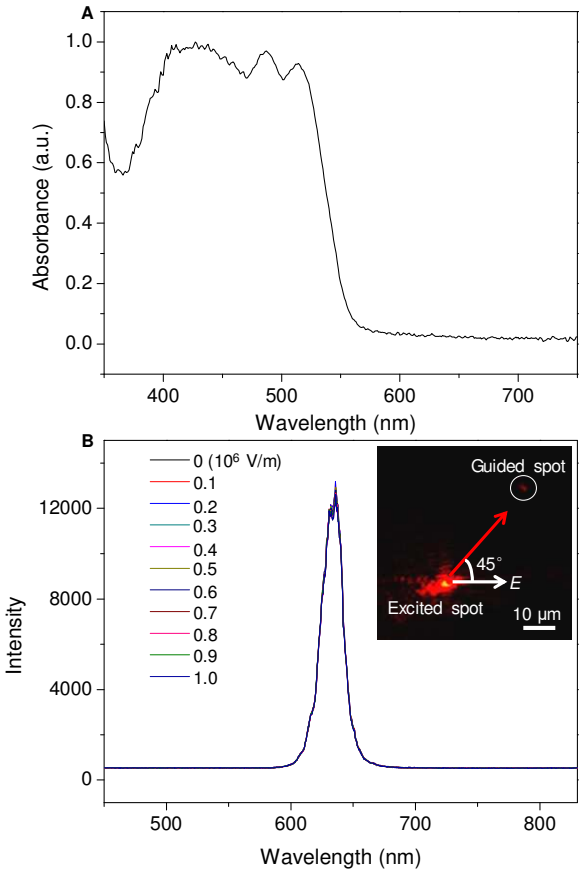

fig. S12. Electric effect on the passively waveguided light. (**A**) The absorption spectrum of BPEA nanowires. (**B**) The emission spectra out-coupled from one tip of the wire under the input of a 635 nm laser signal from the other tip. The applied electric field strength is increased from 0 to 1.0×10^6 V/m. Insert is the microscopy image of the wire under the luminescence of the 635 nm focused laser beam.

From the absorption spectrum of the BPEA nanowires shown in fig. S12A, we can see that the wire cannot be excited by the 635 nm light. Therefore, the incident light should be passively guided in BPEA wire without the formation of excitons, or exciton polaritons. Figure S12B demonstrates a very stable out-coupling of the light signal at around of 635 nm (the broadening of the laser wavelength was caused by the scattering) upon the electric field of different strengths, which verifies that the propagated photons do not response to the electric field, and confirms that the asymmetric photon transport in this work is based on the response of the excitonic portion of the EPs.

section S7. Orientation of BPEA excitons in the molecule-stacked nanostructures

BPEA excitons, as the Frenkel type excitons, are localized in the molecules and exhibit a nature of one-dimensional (1D) transition dipole. Figuring out the direction of the excitons will help us to better understand the mechanism of the electrically induced asymmetric photon transport and to further design photonic elements based on the angular dependence of the transport asymmetry.

Figure S13 displays the spatial relationship between the BPEA molecular transition dipole moment and the growth direction of the BPEA nanowire. The projection of the molecular transition dipole has an angle of 45° to the long wire axis. To further clarify the direction of the transition dipole in the BPEA nanowires, we measured the polarization angle dependent PL spectra as shown in fig. S14. Generally, the specific molecular orientation in organic crystals results in a strong polarization dependent absorption (*48, 49*). Moreover, the PL intensity is at its maximum when the linearly polarized laser is parallel to the dipole moment of the emissive molecule (i.e., long molecular axis) and at its minimum when the linearly polarized laser is perpendicular to the dipole moment (*50*).

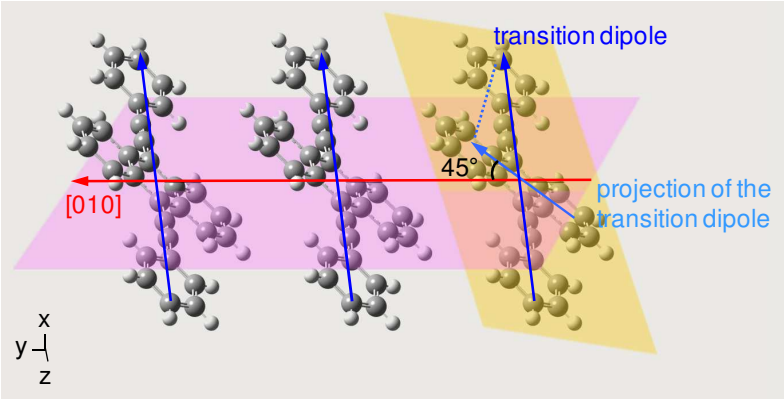

fig. S13. Spatial relationship between the BPEA molecular transition dipole moment (blue arrow) and the [010] growth direction (red arrow) of the BPEA nanowire. The transition dipole of BPEA molecule is aligned transverse to the acene long axis, pointing in the direction of the external phenyl groups (*49*). It can be seen that the projection of transition dipole (light blue arrow) leans an angle of 45° to the long wire axis, which can be further verified by the experimental observation of polarization angle dependent PL intensities as illustrated in fig. S14.

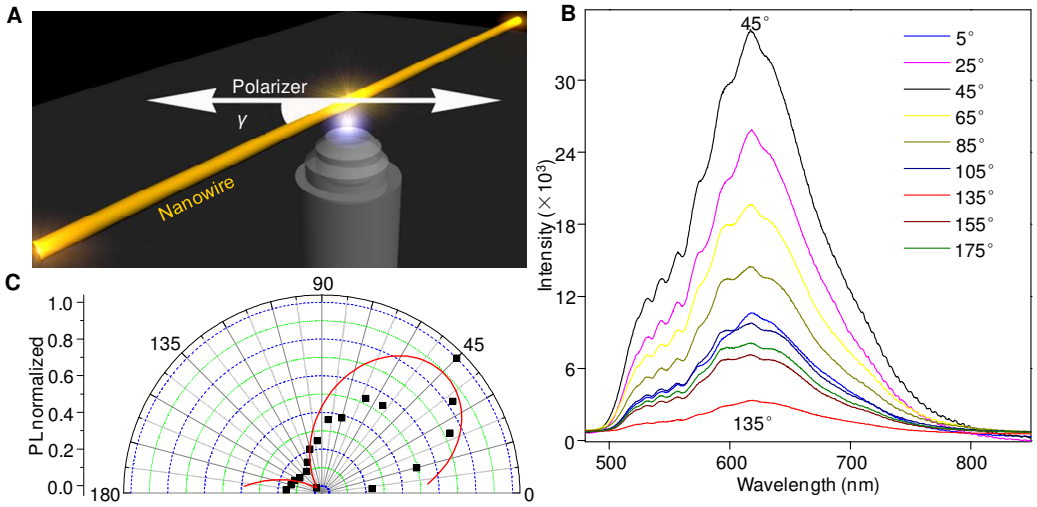

fig. S14. Polarization angle–dependent photoluminescence measurements. (**A**) Schematic illustration of the setup for the polarized excitation. A single wire was excited with a linearly polarized laser beam at the middle part, and the waveguided emissions were detected from the tip. γ refers to the angle between the long axis of the BPEA wire and the incident polarization adjusted by a half-wave plate. (**B**) PL spectra collected by tuning the incident polarization. (**C**) Polar image of the peak PL intensities with varied γ values. Solid red line is the fitted curve in the form of $\cos^2$.

The maximum and minimum values of the PL intensity occur at the polarization angle (γ) of 45° and 135°, respectively. This is a direct consequence of the polarization-dependent absorption, suggesting that the molecular transition dipole leans at an angle of 45° to the preferential growth direction of the nanowires (*35*). Therefore, the photon transport symmetry in the wires can be effectively tuned by changing the angle (α) between the applied electric field and the wire axis, as is demonstrated in the main text. Moreover, the maximum projection of electric field strength on the direction of excitons occurs when the field direction is parallel to the exciton direction, i.e. when the field is applied with an angle (α) of 45°.

section S8. Switching speed and switching frequency measurements for the electrically controlled SPDT optical switch

To analyze the time of the electro-optical response, we applied a series of electric pulses with the rise time of 3.8 ns to the BPEA wire and then measured the modulated optical signal, as shown in fig. S15.

The fast optical-electrical response time facilitates the production of high-frequency switching device. As shown in Fig. 4G, the square-wave electric signals with frequency of 10 MHz were applied to the device and the SPDT switch reveals the same 10 MHz light pulse frequency accordingly. Here, we demonstrate that the switching frequency of the SPDT switch could be further increased under other electric signal frequencies, as illustrated in fig. S16.

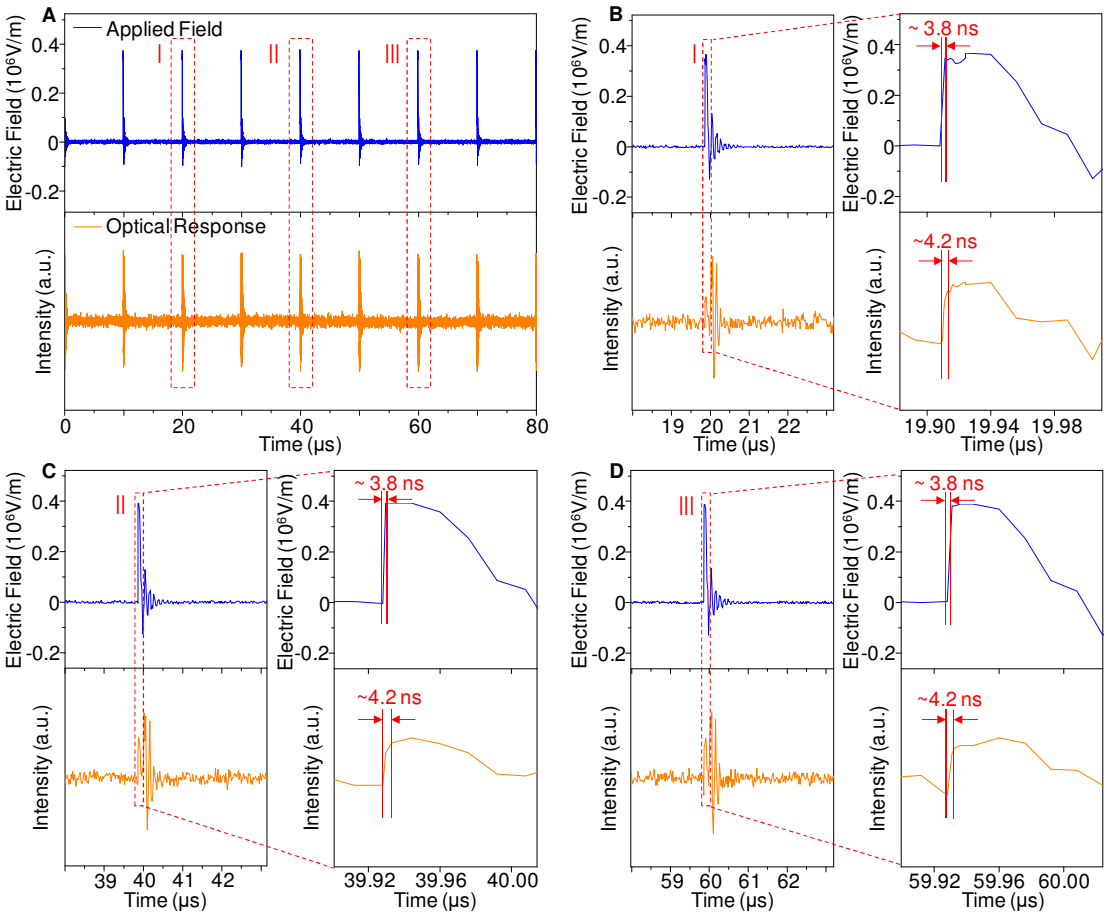

fig. S15. Switching speed measurements for the optical SPDT switch. (**A**) Time-resolved output response of the switch to the applied electric signals. A series of light pulses were modulated by applying electric pulses with frequency of 10^5 Hz and rise time of 3.8 ns. (**B**) to (**D**) Partial enlarged views for three pairs of typical electric pulses and response peaks in (a) to study the stability and reliability of the measurements. The results indicate that the rise time of the applied pulse field is very stable (3.8 ns), and the SPDT switch exhibits a constant response time of 4.2 ns.

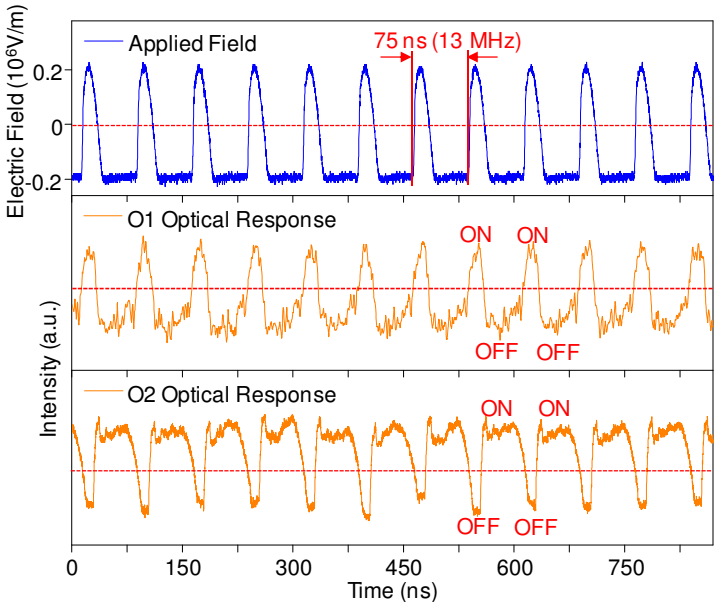

fig. S16. Temporal intensity profiles of O1 and O2 ports in the device shown in Fig. 4 obtained by increasing the frequency of the electric signal to ~13 MHz. A frequency of 13 MHz is demonstrated in the SPDT switch as expected. This indicates again that the frequency of the SPDT switch is completely determined by the performance of the applied electric field, and by further optimizing the electric instrument, we could obtain higher frequency for our SPDT switch.

section S9. Schematic of the experimental measurements

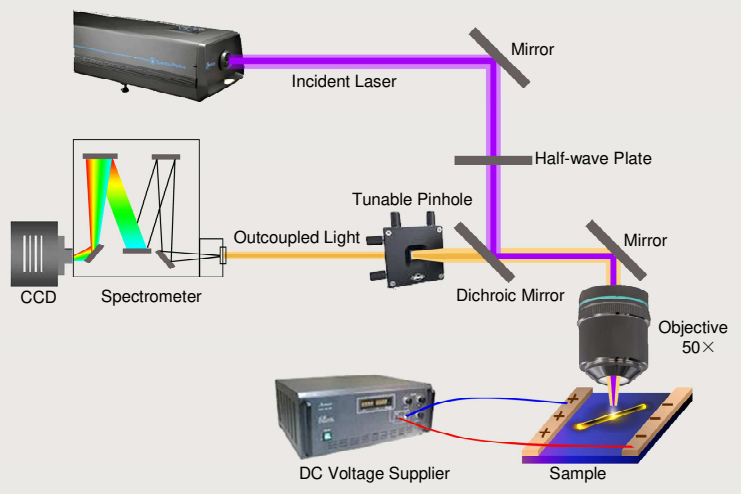

fig. S17. Schematic demonstration of the experimental setup for the steady-state optical measurement. A 351 nm continuous wave argon-ion laser (Spectra-Physics, Beamlok 2065) was used to optically pump the nanowire samples. The pump beam was focused to a 2-μm-diameter spot on the sample by using an objective lens (Nikon CFLU Plan, 50×, N.A.=0.8). The emissions from the individual wires were collected by the same objective and guided to a confocal pinhole. After passing through the pinhole, the optical signal was collected using a grating spectrometer (Acton, SP2300) with a matched thermal-electrically cooled CCD (Princeton Instruments, ProEm: 1600*200B). A commercial DC voltage supplier was used to apply an external electric field for the measurements of field-induced asymmetric optical outcoupling.

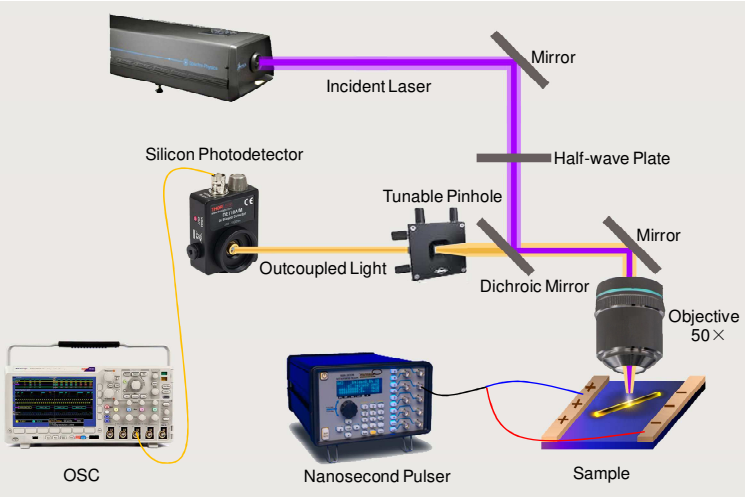

fig. S18. Schematic demonstration of the response time and switching frequency measurement. Laser excitation (351 nm) was focused through the objective lens to a diffraction-limited spot on the nanowire. After the emission of individual wires passed through the pinhole, the signals subject to a pulsed electric field was detected with a Si photodetector and monitored with an oscilloscope. The pulsed electric field was driven by a nanosecond signal generator, which supports tunable amplitude, frequency and rise time.